Energy & Environmental Science

ROYAL SOCIETY OF CHEMISTRY

PAPER

View Article Online
View Journal | View Issue

Cite this: *Energy Environ. Sci.*, 2024, **17**, 2541

High-efficiency unbiased water splitting with photoanodes harnessing polycarbazole hole transport layers†

Jin Wook Yang,[a] Su Geun Ji,[a] Chang-Seop Jeong,[b] Jaehyun Kim,[a] Hee Ryeong Kwon,[a] Tae Hyung Lee,[a] Sol A Lee,[a] Woo Seok Cheon,[a] Seokju Lee,[a] Hyungsoo Lee,[b] Min Sang Kwon,[a] Jooho Moon,*[b] Jin Young Kim*[a] and Ho Won Jang*[ac]

Received 4th October 2023,
Accepted 21st February 2024

DOI: 10.1039/d3ee03353h

rsc.li/ees

The construction of uniform heterojunctions for effective hole transport in a nanoporous $BiVO_4$ photoanode is highly challenging, despite its promise for unbiased photoelectrochemical (PEC) water splitting. Herein, we grew a nanoscale conjugated polycarbazole framework (CPF-TCB) on nanoporous Mo:$BiVO_4$ and exhaustively assessed its hole extraction capability. Type II band alignment in the CPF-TCB/Mo:$BiVO_4$ heterostructure enabled effective hole transport by suppressing charge recombination, enhancing both the fill factor and stability of the photoanode after loading a cocatalyst. The $NiFeCoO_x$/CPF-TCB/Mo:$BiVO_4$ photoanode generates a superlative water oxidation photocurrent density of 6.66 mA cm^{-2} at 1.23 V *versus* the reversible hydrogen electrode. By combining the photoanode with a perovskite photocathode and a perovskite/Si solar cell, two types of PEC tandem devices exhibit solar-to-hydrogen conversion efficiencies of 6.75% and 9.02%, which are the topmost records under tandem illumination mode. This work provides a significant step for designing high-performance organic–inorganic hybrid photoelectrodes for solar hydrogen production.

Broader context

Photoelectrochemical (PEC) water splitting is a promising technology to produce green hydrogen and reduce the carbon footprint. High solar-to-hydrogen (STH) conversion efficiency and long-term stability of tandem devices must be achieved for the commercialization of the PEC approach. Bismuth vanadate ($BiVO_4$), providing a high photovoltage, has been considered an excellent photoanode material for tandem devices, but nanostructuring and hole transport layers (HTL) are necessary to overcome its charge recombination issue. However, it is very challenging not only to explore HTL materials with suitable band structures for $BiVO_4$, but also to uniformly coat it on the nanostructure. Herein, we demonstrate a conjugated polycarbazole framework (CPF-TCB) as a new hole extraction layer for a nanoporous molybdenum-doped $BiVO_4$ photoanode for unassisted solar hydrogen production. The intimately contacted CPF-TCB/Mo:$BiVO_4$ heterostructure forms a type-II band alignment, reinforcing charge separation. After loading a cocatalyst, the $NiFeCoO_x$/CPF-TCB/Mo:$BiVO_4$ photoanode combined with a perovskite photocathode and a perovskite/Si photovoltaic cell affords remarkable STH conversion efficiencies of 6.75% and 9.02%, respectively. The high-performance tandem devices demonstrate the prospective potential of organic–inorganic hybrid photoanodes for unassisted solar hydrogen production.

Introduction

Photoelectrocatalysis, which is more efficient than photovoltaic–electrocatalysis in the manufacturing process and photocatalysis in yield, is highly promising for solar hydrogen production.[1–3] The trade-off between photovoltage and photocurrent based on the band gap of a single photoelectrode requires an electrical bias to exceed the water splitting voltage, which is a challenge in the photoelectrochemical (PEC) approach.[4] To overcome this challenge, unassisted water splitting using tandem devices comprising dual light absorbers has

[a] *Department of Materials Science and Engineering, Research Institute of Advanced Materials, Seoul National University, Seoul 08826, Republic of Korea. E-mail: jykim.mse@snu.ac.kr, hwjang@snu.ac.kr*
[b] *Department of Materials Science and Engineering, Yonsei University, Seoul 03722, Republic of Korea. E-mail: jmoon@yonsei.ac.kr*
[c] *Advanced Institute of Convergence Technology, Seoul National University, Suwon 16229, Republic of Korea*

† Electronic supplementary information (ESI) available. See DOI: https://doi.org/10.1039/d3ee03353h

been attempted to maximize photovoltage *via* light harvesting.[5] In terms of solar-to-hydrogen (STH) conversion efficiency for tandem devices, bismuth vanadate ($BiVO_4$) is an essential photoanode material owing to its suitable band gap, enabling both high photovoltage and absorption spectrum separation with posterior absorber materials.[6] Nevertheless, a short carrier diffusion length ($\sim$70 nm) incurs charge recombination,[7] lowering its photocurrent density far below the theoretical value of 7.5 mA cm^{-2}.

In addition to the nanostructuring of $BiVO_4$ to reduce the diffusion path, it is necessary to introduce charge transport layers to reinforce charge separation.[8] Specifically, since hole transport is more susceptible to being blocked by potential barriers along the carrier passage, it is necessary to develop a competent hole transport layer (HTL) to improve the fill factor (FF) of $BiVO_4$ in order to secure high operating points of tandem devices. Unlike the various metal oxides, such as SnO_2,[9] WO_3,[10] TiO_2,[11] and In_2O_3,[12] that plainly construct type II band alignments favorable to electron transport under $BiVO_4$, the inorganic material pool for HTL is highly limited. Owing to its stringent requirements such as a low band gap, high durability, and more negative conduction band edge than that of $BiVO_4$, only few types of research on HTL have been reported. Quantum dot synthesis from carbon[13] and black phosphorous[14] or elemental doping for carbon nitride[15] has been attempted to form staggered band edges onto $BiVO_4$. Although these 2-step approaches of coating after phase formation are advantageous for ensuring conductivity, possible degeneration in PEC performances by clogging the pores of nanostructured $BiVO_4$ or blocking light also exists.

Conjugated polymers have been widely investigated in organic photovoltaics[16] and perovskite solar cells.[17] Their fascinating nature of tailored band structures stems from the diversity of functional groups.[18] In addition, high electrical conductivity is retained without post-processing since the π-electrons delocalized by alternating single bonds and double bonds facilitate charge flow.[19] These delocalized electrons in the π-conjugated backbone also contribute to electrochemical stability by preventing charge accumulation. Despite these favorable features for HTL, few studies have been applied to nanostructured photoelectrodes owing to the difficulty of their direct growth without reducing the specific surface area. Forming a heterojunction between nanoporous $BiVO_4$ and conjugated polymers with optimal band structures through conformal growth provides a breakthrough to the chronic issues in the efficiency and durability of photoanodes.

Here, we demonstrate the hole extraction of a conjugated polycarbazole framework (CPF-TCB) layer on the nanoporous molybdenum-doped $BiVO_4$ (Mo:$BiVO_4$) photoanode. Electropolymerization is utilized to conformally deposit CPF-TCB on Mo:$BiVO_4$ by elaborately controlling the growth *via* sweep cycle, and their uniform thickness is identified by transmission electron microscopy (TEM). After coating a tannic acid-based $NiFeCoO_x$ cocatalyst, the $NiFeCoO_x$/CPF-TCB/Mo:$BiVO_4$ photoanode exhibits exceptional PEC water oxidation with a high photocurrent density of 6.66 mA cm^{-2} at 1.23 V *versus* a reversible hydrogen electrode (V_{RHE}). X-ray spectroscopic analyses reveal the electronic environment of CPF-TCB/Mo:$BiVO_4$, and density functional theory (DFT) calculations suggest a theoretical basis for the charge transport within the heterojunction. Systematic studies on the charge carrier dynamics verify the hole transport capability of CPF-TCB, and confirm that the enhanced PEC performances originate from the type II band structures. For unbiased solar hydrogen production, two types of PEC tandem devices using the $NiFeCoO_x$/CPF-TCB/Mo:$BiVO_4$ photoanode with a perovskite photocathode and a perovskite/Si solar cell are fabricated. These tandem devices measured under tandem illumination mode (mode T) attain excellent STH conversion efficiencies of 6.75% and 9.02%, respectively, which are the foremost records among not only $BiVO_4$-based, but also mode T tandem devices. This study reveals that CPF-TCB is a key material in photoanodes for high-efficiency and high-durability PEC tandem devices.

Results and discussion

The fabrication processes of photoanodes are schematically illustrated in Fig. S1 (ESI†). All designs of the photoanode were carried out with a focus on efficiently separating and transferring charges generated in $BiVO_4$. Firstly, $BiVO_4$ was synthesized from electrodeposited BiOI nanoplates as a precursor to possess nanopores, providing a large specific surface area and short diffusion path.[6] During the annealing process, the removal of surface trap sites in $BiVO_4$ was induced by molybdenum doping.[15] For maximization of the surface area and electron extraction, vertical nanorod-type SnO_2 was introduced as an electron transport layer (ETL) under the photoanode.[9] The thin CPF-TCB layer was directly synthesized onto the surface of Mo:$BiVO_4$ using electropolymerization, and the CPF-TCB/Mo:$BiVO_4$ photoanode was dip-coated with tannic acid-based $NiFeCoO_x$ acting as a cocatalyst. Conformal coating of conductive polymers on $BiVO_4$ without filling its nanopores is highly challenging. As illustrated in Fig. 1(a), the electropolymerization we adopted is sophisticated in that the monomers can intimately contact all surfaces of the photoanode. As a building block to construct the conjugated polycarbazole framework, we employed 1,3,5-tris(*N*-carbazolyl)benzene (TCB) which contains carbazole. Among various aromatic units, such as benzene, thiophene, and pyridine, carbazole applied in the conjugated polymer backbone contributes to the electrochemical stability because of its electrophilic substitution in the nitrogen atom and the aromatic ring.[20,21] The CPF-TCB films were electropolymerized on the Mo:$BiVO_4$ photoanode by linear sweep voltammetry, and their thickness was controlled by the sweep cycle. In the current density–potential (*J*–*V*) curves (Fig. S2, ESI†), increases in the current density were observed around 1.2 V as the sweep number increased. This indicates that as the monomers polymerized, the formed larger frameworks increased the number of sites where additional monomers could attach.[22] We observed that the bright yellowish Mo:$BiVO_4$ surfaces became cloudy after polymerization, and also

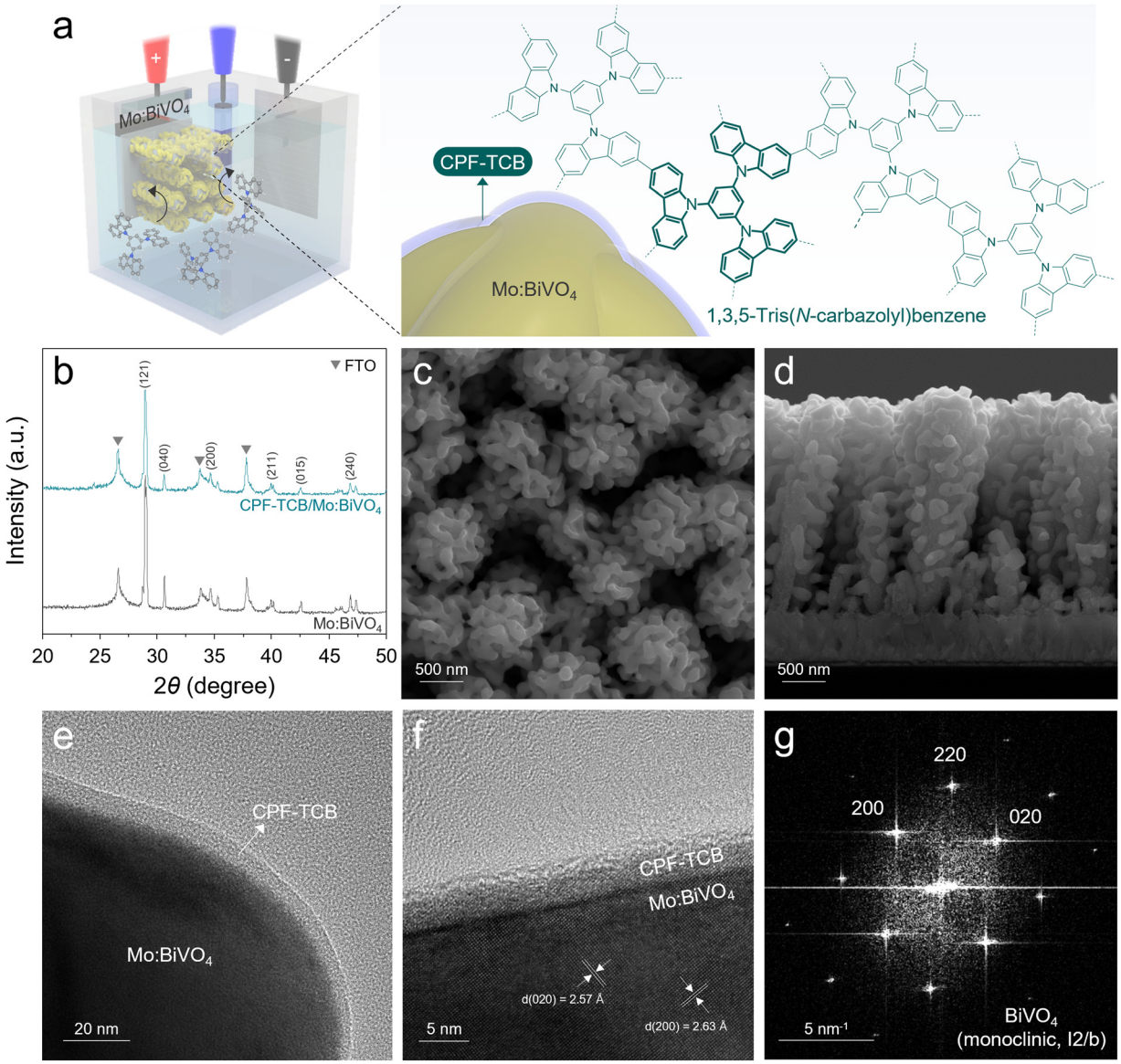

Fig. 1 Structural characterization. (a) Schematic illustration of the electropolymerization of CPF-TCB on Mo:$BiVO_4$. (b) XRD of Mo:$BiVO_4$ and CPF-TCB/Mo:$BiVO_4$. (c) Top-view and (d) cross-sectional SEM images of CPF-TCB/Mo:$BiVO_4$. (e) TEM and (f) HRTEM images of CPF-TCB/Mo:$BiVO_4$. (g) FFT pattern of monoclinic Mo:$BiVO_4$.

confirmed a color change to yellow when coated on the fluorine-doped tin oxide (FTO), as shown in Fig. S3 (ESI†).

The X-ray diffraction (XRD) patterns in Fig. 1(b) were indexed to monoclinic $BiVO_4$ (PDF# 04-010-5173), showing that the crystal structure of $BiVO_4$ was unchanged after deposition of CPF-TCB. In the top field-emission scanning electron microscopy (FESEM) image of CPF-TCB/Mo:$BiVO_4$ (Fig. 1(c)), the coexistence of nanopores and ETL-derived mesopores was observed, leading to the maximized surface area of the photoanode. The overall morphology of the 2.5 μm-thick vertical photoanode suitable for light absorption was confirmed through the cross-sectional FESEM image (Fig. 1(d)). Since the CPF-TCB thin layer with optimal sweep cycle was indistinguishable, we prepared Mo:$BiVO_4$ with 40 time-swept CPF-TCB. As exhibited in Fig. S4 (ESI†), even at high cycle numbers, the CPF-TCB layer was uniformly coated on Mo:$BiVO_4$ without agglomeration and clogging of nanopores. The corresponding energy dispersive X-ray (EDX) mapping indicated the uniform distribution of C and N elements from CPF-TCB on the $BiVO_4$ surface. The CPF-TCB film with the optimal sweep cycle was revealed in the TEM image. As shown in Fig. 1(e), the CPF-TCB thin layer conformally covered Mo:$BiVO_4$. The high-resolution TEM (HRTEM) image (Fig. 1(f)) showed that under the optimal sweep cycle, CPF-TCB grew uniformly onto Mo:$BiVO_4$ with a thickness of 5 nm. The amorphous nature of CPF-TCB was consistent with the characteristics of electropolymerized polycarbazole frameworks in previous studies,[22,23] and also corresponded to the XRD results showing no

difference before and after deposition (Fig. 1(b)). The lattice fringes with interplanar spacings of 2.57 and 2.63 Å in two directions correspond to the (020) and (200) planes, respectively. The fast Fourier transformation (FFT) patterns in Fig. 1(g) show the diffraction spots for the (200) and (020) planes, indicating the crystalline monoclinic phase (*I*2/*b* group). These results matched well with the XRD analysis, identifying the suitable phase for water oxidation.[24]

The photoelectrochemical water oxidation of the fabricated photoanodes was evaluated in a three-electrode cell with 1 M potassium borate ($K–B_i$) buffer (pH 9.5) under AM1.5G solar illumination. To investigate the optimal thickness of the CPF-TCB layer for Mo:$BiVO_4$, the electropolymerization of CPF-TCB was executed with different sweep cycles (5, 10, and 20 cycles). In the *J*–*V* curves of the CPF-TCB/Mo:$BiVO_4$ photoanodes (Fig. S5, ESI†), they exhibited similar photocurrent densities at 1.23 V_{RHE}, whereas CPF-TCB with 10 cycles exhibited the largest polarization. This indicated effective charge separation, and it was confirmed to grow to a thickness of 5 nm under 10 cycles (Fig. 1(f)). The PEC characteristics of Mo:$BiVO_4$ before and after the 10-cycle deposition of the CPF-TCB layer were evaluated with and without the $NiFeCoO_x$ cocatalyst. The *J*–*V* curves for four types of photoanodes are presented in Fig. 2(a). The photocurrent density of CPF-TCB/Mo:$BiVO_4$ was measured to 3.82 mA cm^{-2} at 1.23 V_{RHE}, which is higher than that of Mo:$BiVO_4$ (3.30 mA cm^{-2}). The improvement was more pronounced with the cocatalyst, with $NiFeCoO_x$/CPF-TCB/Mo:$BiVO_4$ reaching a remarkable photocurrent density of 6.66 mA cm^{-2} at 1.23 V_{RHE}, which is higher than that of $NiFeCoO_x$/Mo:$BiVO_4$ (6.09 mA cm^{-2}). This means that CPF-TCB contributes to effective hole transport from Mo:$BiVO_4$ to the cocatalyst. To verify the exceptional photocurrent density, linear sweep voltammetry (LSV) measurements of five $NiFeCoO_x$/CPF-TCB/Mo:$BiVO_4$ photoanodes fabricated by the same process were conducted. Fig. S6 (ESI†) shows a minor variation in PEC performances between samples, indicating that the $NiFeCoO_x$/CPF-TCB/Mo:$BiVO_4$ photoanode has good reproducibility. As shown in the SEM images of $NiFeCoO_x$/CPF-TCB/Mo:$BiVO_4$ (Fig. S7, ESI†), no structural changes were observed in the photoanode before and after the LSV measurement, indicating that CPF-TCB and $NiFeCoO_x$ effectively protect Mo:$BiVO_4$ and promote water oxidation. The resulting significant enhancement in 0.4 ∼ 0.8 V_{RHE} is advantageous to provide high power at the general range of the operating point in PEC tandem devices.[25] The contribution of CPF-TCB to the power of the photoanode was quantitatively evaluated by the fill factor, as shown in Fig. 2(b). It is noteworthy that the maximum power point with the CPF-TCB layer was achieved at a more cathodic potential of 0.65 V_{RHE} compared to that without the layer (0.75 V_{RHE}), indicating that CPF-TCB served to elevate both photocurrent and photovoltage. Based on the rectangularity at the maximum power point, we calculated the FF of the photoanodes using the following equation:

$$FF\ (\%) = [J_{MP}(1.23 - V_{MP})]/[J_{SC}(1.23 - V_{ON})]$$

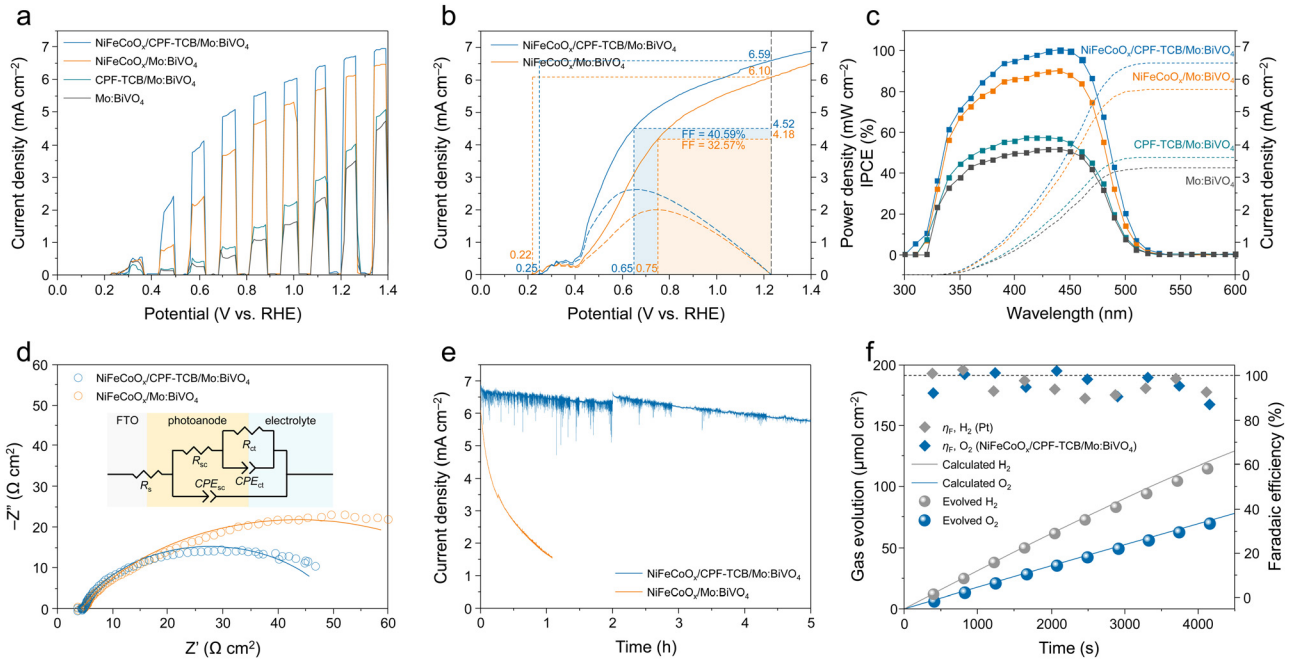

Fig. 2 Photoelectrochemical water oxidation. (a) *J*–*V* curves of Mo:$BiVO_4$, CPF-TCB/Mo:$BiVO_4$, $NiFeCoO_x$/Mo:$BiVO_4$, and $NiFeCoO_x$/CPF-TCB/Mo:$BiVO_4$ photoanodes. (b) Fill factors of $NiFeCoO_x$/Mo:$BiVO_4$ and $NiFeCoO_x$/CPF-TCB/Mo:$BiVO_4$ photoanodes. (c) IPCE at 1.23 V_{RHE} and integrated current density of the Mo:$BiVO_4$, CPF-TCB/Mo:$BiVO_4$, $NiFeCoO_x$/Mo:$BiVO_4$, and $NiFeCoO_x$/CPF-TCB/Mo:$BiVO_4$ photoanodes. (d) EIS Nyquist plots at 0.5 V_{RHE} and (e) *J*–*t* curves at 1.23 V_{RHE} of the $NiFeCoO_x$/Mo:$BiVO_4$ and $NiFeCoO_x$/CPF-TCB/Mo:$BiVO_4$ photoanodes. (f) Faradaic efficiency and gas evolution at 1.23 V_{RHE} of the $NiFeCoO_x$/CPF-TCB/Mo:$BiVO_4$ photoanodes. All measurements were conducted in $K–B_i$ buffer (pH 9.5) under AM1.5G 1 sun illumination.

where J_{MP} and V_{MP} are the current density and potential at the maximum power point, respectively, J_{SC} is the current density at 1.23 V_{RHE}, and V_{ON} is the onset potential. When the CPF-TCB layer was inserted between $NiFeCoO_x$ and Mo:$BiVO_4$, the FF increased from 32.57% to 40.59%. The improvement in power efficiency makes application to PEC tandem devices more advantageous. The photoactivities of photoanodes were also verified by the incident photon-to-current conversion efficiency (IPCE) measured at 1.23 V_{RHE} (Fig. 2(c)). In photoanodes containing CPF-TCB, the increases in IPCE were confirmed in the wavelength range below 500 nm, regardless of the presence of the cocatalyst. Especially, the maximum value of $NiFeCoO_x$/CPF-TCB/Mo:$BiVO_4$ was improved by 10% compared to $NiFeCoO_x$/Mo:$BiVO_4$, achieving near-complete IPCE near 450 nm. The IPCE spectra were integrated with photon flux over wavelength to revalidate the current density. The integrated photocurrent densities of all four types of photoanode practically matched the current density in the *J–V* curves (Fig. 2(a)).

The hole extraction ability of CPF-TCB was further proven by electrochemical impedance spectroscopy (EIS) measurements conducted at 0.5 V_{RHE}, where large photoactivity differences appeared. The Nyquist plots were fitted with an equivalent circuit as indicated in Fig. 2(d), and their values are tabulated in Table S1 (ESI†). The charge transfer resistance (R_{ct}) of $NiFeCoO_x$/CPF-TCB/Mo:$BiVO_4$ (41.45 Ω cm^2) was similar to that of $NiFeCoO_x$/Mo:$BiVO_4$ (42.65 Ω cm^2), showing the same charge injection of the cocatalyst. For the charge transport resistance (R_{sc}) in the photoanode, N i$FeCoO_x$/CPF-TCB/Mo:$BiVO_4$ had a lower value of 5.525 Ω cm^2 compared to $NiFeCoO_x$/Mo:$BiVO_4$ (36.13 Ω cm^2). The significant decrease in R_{sc} indicates that the enhancement of the PEC performance sprang from the hole extraction behavior of CPF-TCB. The durability of the photoanodes was examined by chronoamperometry at 1.23 V_{RHE}. As shown in the current density–time (*J–t*) curves (Fig. 2(e)), the $NiFeCoO_x$/CPF-TCB/Mo:$BiVO_4$ photoanode ran stably for 5 h, whereas the $NiFeCoO_x$/Mo:$BiVO_4$ photoanode exhibited a sharp degradation within 1 h. This means that CPF-TCB plays a role as the protective layer as well as the HTL for Mo:$BiVO_4$. The improved stability is also indirect evidence of the efficient hole extraction of CPF-TCB. The instability of the photoanode is derived from the hole accumulation causing self-oxidation of $BiVO_4$. The expedited charge separation by CPF-TCB prevents the hole accumulation, enhancing the PEC stability. Furthermore, gas chromatography was conducted to collect the evolved gas and measure the faradaic efficiency. As shown in Fig. 2(f), faradaic efficiencies of nearly 100% were acquired in both the $NiFeCoO_x$/CPF-TCB/Mo:$BiVO_4$ photoanode and Pt cathode, indicating that generated charges were fully consumed for oxygen and hydrogen evolution. It was also confirmed that the actual gas evolution rates were close to the calculated values.

The formation of the CPF-TCB layer was further proved by Fourier transform-infrared (FT-IR) spectroscopy, as shown in Fig. 3(a). Within the wavenumber range of 1000 to 1800 cm^{-1} where typical polymer bonding is observed, no peaks were observed for Mo:$BiVO_4$. On the other hand, several peaks were identified in CPF-TCB/Mo:$BiVO_4$, among which peaks at 1223, 1329, 1438, 1462, and 1591 cm^{-1} were found to originate from the carbazole functional group in CPF-TCB. These spectra most directly verify that the amorphous CPF-TCB thin film was well formed on Mo:$BiVO_4$. To further demonstrate the charge transport behavior of CPF-TCB and the resulting changes in the electronic states of Mo:$BiVO_4$, X-ray absorption spectroscopy (XAS) was employed for the V K-edge of Mo:$BiVO_4$ with and without CPF-TCB. In the Fourier-transformed extended X-ray absorption fine structure (EXAFS) spectra (Fig. S8, ESI†), the peak corresponding to V–O bonding was observed around 1.3 Å for both samples, confirming that CPF-TCB had no influence on the interatomic structure of Mo:$BiVO_4$. X-ray absorption near edge structure (XANES) spectra for the V K-edge in Fig. 3(b) show the electronic state changes. After forming the CPF-TCB layer on Mo:$BiVO_4$, the pre-edge peak shifted from 5469.4 to 5469.8 eV, and the edge peak shifted from 5501.4 to 5502.6 eV. The prominent shifts indicate the relative electron transport towards Mo:$BiVO_4$ due to charge separation caused by the hole extraction of CPF-TCB.[26]

X-ray photoelectron spectroscopy (XPS) analysis of Mo:$BiVO_4$, CPF-TCB, and their heterojunction was carried out to scrutinize the electronic structures, and the wide spectra are presented in Fig. S9 (ESI†). As shown in Fig. 3(c), after the deposition of CPF-TCB, the V $2p_{1/2}$ and $2p_{3/2}$ peaks shifted from 523.53 and 516.13 eV to the higher binding energies of 523.86 and 516.56 eV, respectively. The Bi $4f_{5/2}$ and $4f_{7/2}$ peaks also shifted from 163.83 and 158.53 eV to the higher binding energies of 164.16 and 158.86 eV, respectively (Fig. S10, ESI†). In contrast, the N 1s peak (400.20 eV) in carbazole slightly moved to the lower binding energy of 400.16 eV, as exhibited in Fig. 3(d). These tendencies in the binding energy are attributed to the strong interfacial interactions between CPF-TCB and Mo:$BiVO_4$.[27,28] Depth profiling was performed while etching the surface of CPF-TCB/Mo:$BiVO_4$ by irradiating Ar plasma with time variation. The N 1s peak intensity gradually decreased over time and completely disappeared after 10 min plasma, indicating that the 5 nm-thick CPF-TCB layer was etched in 10 min. On the other hand, the V 2p peak intensity remained constant after a slight decrease over time, and the Bi 4f peaks maintained high intensity regardless of time. The transition of peak positions during etching was ascribed to the change in the interaction between CPF-TCB and Mo:$BiVO_4$. Meanwhile, the final $NiFeCoO_x$/CPF-TCB/Mo:$BiVO_4$ photoanode was also analyzed by XPS, as shown in Fig. S11 (ESI†). The compositional elements of the cocatalysts were revealed in the Ni 2p (873.3 and 855.6 eV for $2p_{1/2}$ and $2p_{3/2}$), Fe 2p (724.3 and 710.9 eV for $2p_{1/2}$ and $2p_{3/2}$), and Co 2p (796.5 and 781.8 eV for $2p_{1/2}$ and $2p_{3/2}$) spectra. The C 1s peak was deconvoluted into three peaks representing the C═O (288.6 eV), C–O (285.5 eV), and C–C (284.5 eV) bondings, which were derived from the tannic acid chelating metal ions.[29] Metal–(hydro)oxide bondings (M–O and M–OH) that appeared in the deconvoluted O 1s peaks were also attributed to the cocatalyst.[30]

To theoretically scrutinize the charge transport behavior within the CPF-TCB/Mo:$BiVO_4$ heterostructure, DFT calculations were

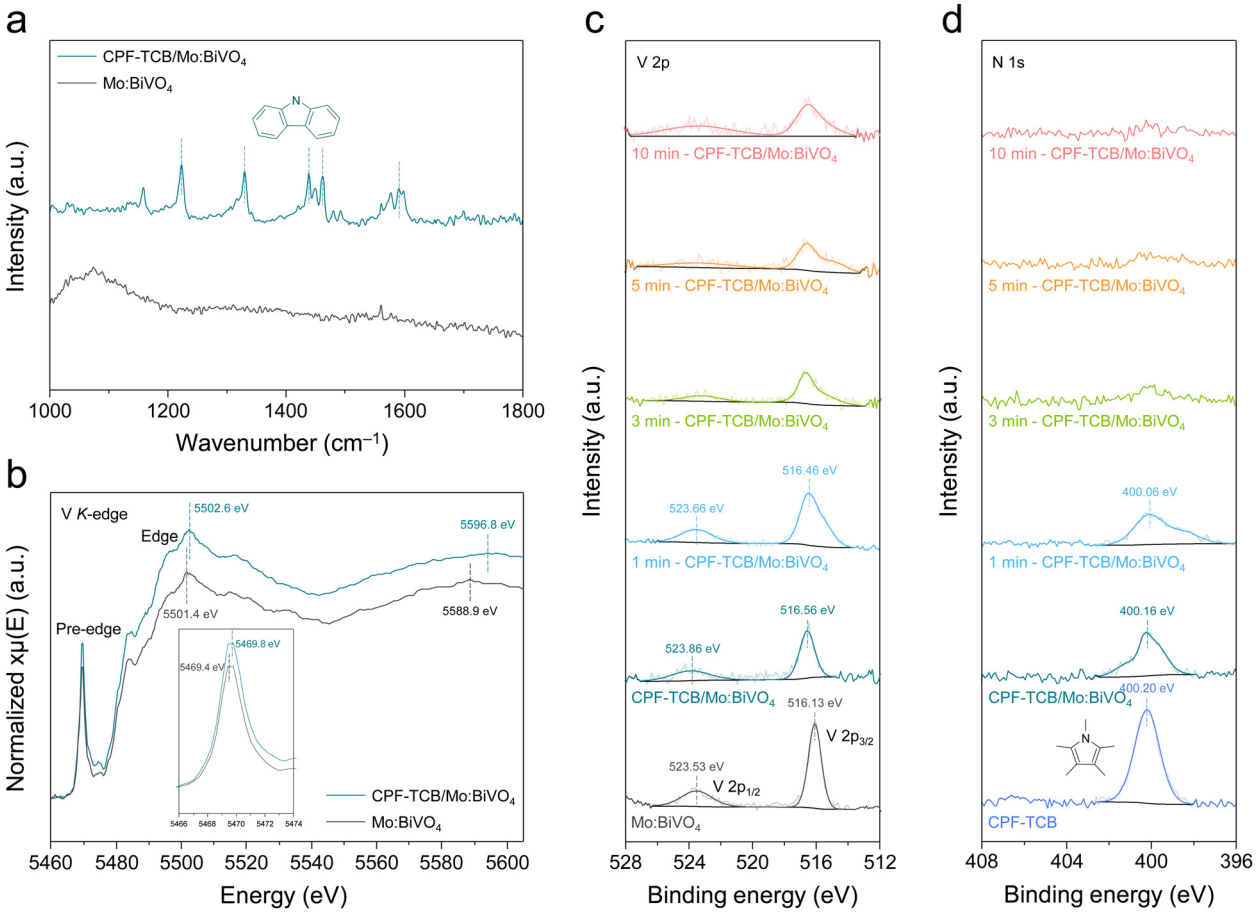

Fig. 3 Spectroscopic analyses of the conjugated polycarbazole frameworks. (a) FT-IR spectra of Mo:$BiVO_4$ and CPF-TCB/Mo:$BiVO_4$. (b) V K-edge XANES spectra of Mo:$BiVO_4$ and CPF-TCB/Mo:$BiVO_4$. (c) V 2p XPS spectra of Mo:$BiVO_4$ and CPF-TCB/Mo:$BiVO_4$ with different Ar plasma etching times. (d) N 1s XPS spectra of CPF-TCB and CPF-TCB/Mo:$BiVO_4$ with different Ar plasma etching times.

utilized. As suggested in Fig. S12 (ESI†), a single layer of CPF-TCB positioned on the (010) surface of $BiVO_4$ was established as the DFT calculation model to elucidate the spatial distribution of charge density differences. Fig. 4(a) shows the 3-dimensional charge density difference across the CPF-TCB/Mo:$BiVO_4$ interface. The charge redistribution mainly occurred at the interface of CPF-TCB/Mo:$BiVO_4$, and electrons accumulated around the surface of Mo:$BiVO_4$. It is one piece of evidence indicating favorable charge transport at the interface of the heterostructure, which is consistent with the aforementioned results of XAS and XPS analysis.[23,31] Additionally, the planar-averaged charge density difference along the *z*-direction normalized to the CPF-TCB/Mo:$BiVO_4$ heterostructure was calculated to investigate quantitative changes (Fig. 4(b)). Strong charge accumulation on the surface of Mo:$BiVO_4$ indicates that electrons are mainly transported from CPF-TCB to Mo:$BiVO_4$ at their interface. According to Bader charge analysis, about 0.05 electrons per supercell are transported from the CPF-TCB layer to Mo:$BiVO_4$ (010). After reaching the equilibrium state, a built-in electric field is developed by the net charge accumulation across the CPF-TCB/$BiVO_4$ heterostructure, promoting charge separation.[32] Thereby, these calculations provide support for

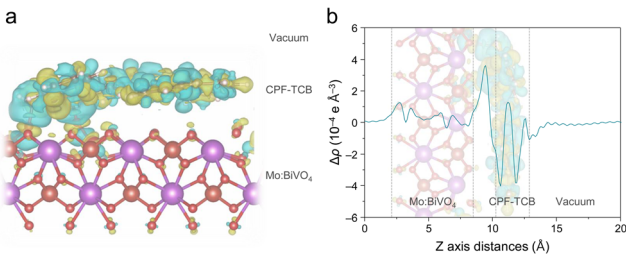

Fig. 4 DFT calculations. (a) Charge density difference across CPF-TCB/Mo:$BiVO_4$. (b) Planar-averaged charge density difference $\Delta\rho$ ($\Delta\rho = \rho_{junction} - \rho_{BiVO_4} - \rho_{CPF\text{-}TCB}$) along the *z*-direction for CPF-TCB/$BiVO_4$.

the crucial charge transport role of CPF-TCB shown in PEC measurements.

The hole extraction capability of CPF-TCB was further demonstrated by Mott–Schottky (M–S) analysis under light-off. Comparing the M–S plots shown in Fig. 5(a), the flat band potentials of TCB/Mo:$BiVO_4$ and Mo:$BiVO_4$ were almost identical. It was in line with the *J*–*V* curves in Fig. 2(a), where there was no difference in the onset potential of the two photoanodes. However, the slope of CPF-TCB/Mo:$BiVO_4$ was lower

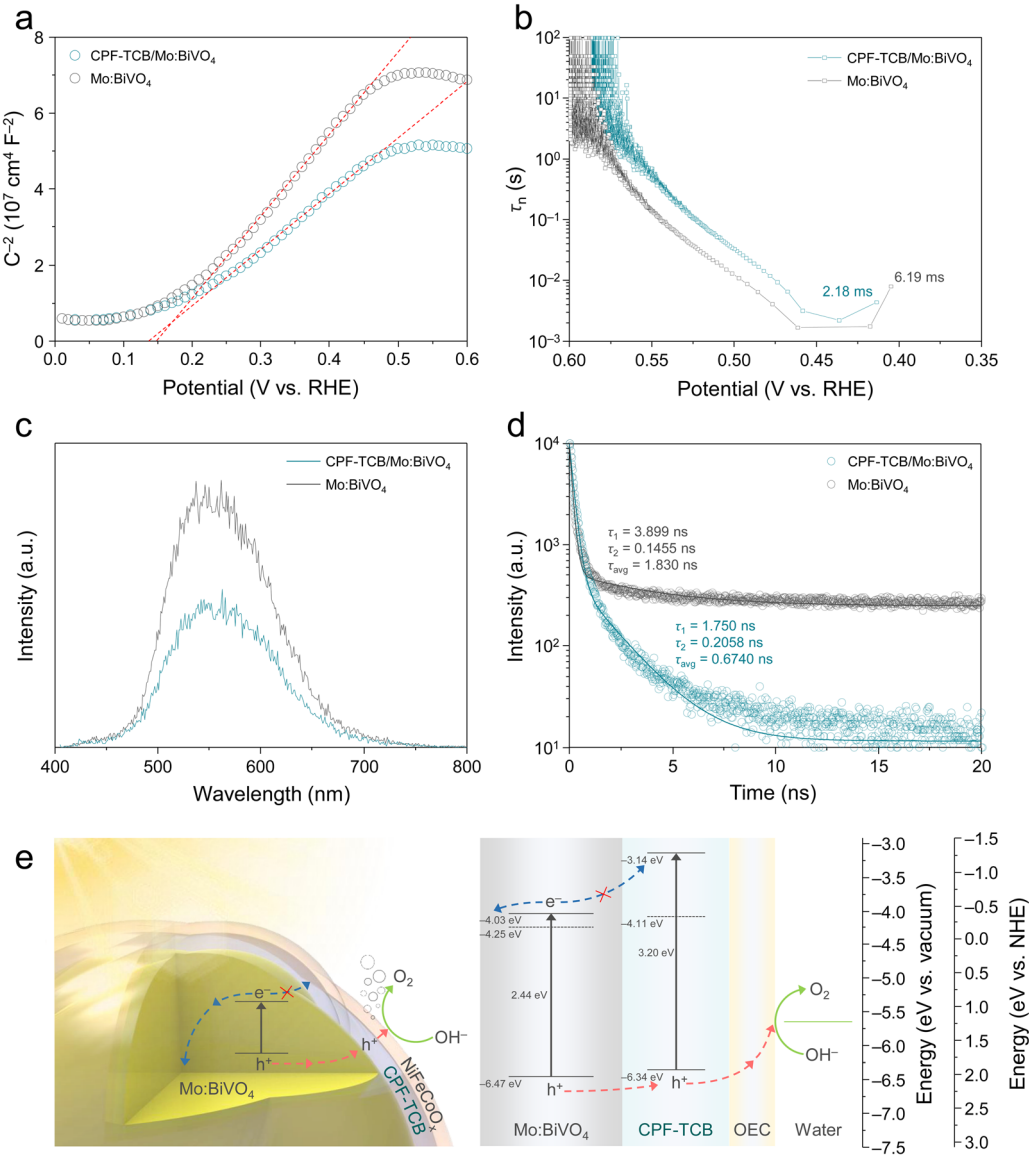

Fig. 5 Charge carrier dynamics. (a) M–S plots of Mo:$BiVO_4$ and CPF-TCB/Mo:$BiVO_4$. (b) OCP-derived carrier lifetimes of Mo:$BiVO_4$ and CPF-TCB/Mo:$BiVO_4$. (c) Steady-state and (d) time-resolved PL of Mo:$BiVO_4$ and CPF-TCB/Mo:$BiVO_4$. (e) Energy band diagram of CPF-TCB/Mo:$BiVO_4$.

than that of Mo:$BiVO_4$, indicating that the donor density (N_D) of Mo:$BiVO_4$ increases when it forms a heterojunction with CPF-TCB. The donor density was calculated by the following equation and tabulated in Table S2 (ESI†):

$$C^{-2} = (2/\varepsilon\varepsilon_0 A^2 e N_D)[V - E_{FB} - (k_B T)/e]$$

where C is the capacitance of the space charge layer (F), ε is the dielectric constant ($\sim$68), ε_0 is the permittivity of the vacuum (8.854×10^{-12} F m^{-1}), A is the surface area (m^2), e is the electron charge (1.062×10^{-19} C), V is the applied potential (V), E_{FB} is the flat band potential (V), k_B is the Boltzmann constant (1.381×10^{-23} F m^{-1}), and T is the temperature (298 K). The higher donor density of CPF-TCB/Mo:$BiVO_4$ (2.125×10^{20} cm^{-3}) than that of Mo:$BiVO_4$ (1.438×10^{20} cm^{-3}) indicates that CPF-TCB enhanced the charge separation as the HTL. The open circuit potential (OCP) transient decay profile is a powerful tool, providing information about the behavior of charges induced by the photovoltage.[33] As shown in the normalized OCP profiles (Fig. S13, ESI†), the CPF-TCB/Mo:$BiVO_4$ photoanode exhibited faster decay than Mo:$BiVO_4$ under light-off. The faster decay profile is caused by the rapid relaxation of charge carriers in the elimination of the illumination, conversely indicating the boosted charge separation under illumination. The carrier lifetime (τ_n) was quantified by the following equation:

$$\tau_n = -[(k_B T)/e](\mathrm{dOCP}/\mathrm{d}t)^{-1}$$

where dOCP/dt is the time derivative of the OCP transient decay. As presented in Fig. 5(b), the carrier lifetime of CPF-TCB/Mo:$BiVO_4$ is 2.18 ms, which is shorter compared to 6.18 ms for Mo:$BiVO_4$. The faster decay time is indicative of

the larger charge recombination after light-off, indicating the expedited charge separation of the heterojunction under illumination.[34,35]

To make a comparison of the charge recombination behavior in the two $BiVO_4$-based photoanodes, photoluminescence (PL) analysis was executed. Fig. 5(c) shows the steady-state PL spectra of Mo:$BiVO_4$ with and without CPF-TCB, displaying peaks at 550 nm originating from radiative charge recombination. The PL emission was intensively quenched in forming a CPF-TCB/Mo:$BiVO_4$ heterojunction, meaning that the HTL suppressed the intrinsic radiative recombination of charges in Mo:$BiVO_4$.[36] The benefit of the heterojunction was further supported by time-resolved photoluminescence (TRPL), elucidating the charge carrier kinetics (Fig. 5(d)). The decay obtained at the PL peak of 550 nm was fitted by the biexponential decay model as shown below, offering two carrier lifetimes (τ_1 and τ_2).

$$I(t) = A_1 e^{-t/\tau_1} + A_2 e^{-t/\tau_2}$$

where I and A are the intensity and amplitude, respectively. As tabulated in Table S3 (ESI†), the τ_2 values associated with non-radiative decay caused by trap sites were similar (0.2058 ns and 0.1455 ns). However, the radiative recombination-related τ_1 of CPF-TCB/Mo:$BiVO_4$ (1.750 ns) was shorter than that of Mo:$BiVO_4$ (3.8 99 ns). The average carrier lifetime (τ_{avg}) also decreased from 1.830 to 0.6740 ns after depositing CPF-TCB. These lifetime drops denote the expeditious extraction of photoexcited holes by CPF-TCB as a hole transport layer.[37]

The fundamental cause of effective charge separation in CPF-TCB/Mo:$BiVO_4$ was disclosed in the band structure analysis. Ultraviolet-visible (UV-vis) spectroscopy was measured, and the absorption spectra calculated by the measured transmittance and reflectance were converted to Tauc plots, as shown in Fig. S14 (ESI†). The optical band gaps of Mo:$BiVO_4$ and CPF-TCB were 2.44 and 3.20 eV, respectively. Ultraviolet photoelectron spectroscopy (UPS) was utilized to precisely determine the work functions and band edge positions, as suggested in Fig. S15 (ESI†). The secondary electron emission (SEE) spectra revealed the work function of Mo:$BiVO_4$ (4.25 eV) and CPF-TCB (4.11 eV) from the difference with the source energy. From the valence band (VB) spectra in the low binding energy region, the energy differences between the Fermi level and VB maximum were verified. The band structure of CPF-TCB/Mo:$BiVO_4$ was constructed by combining UV-vis spectra and UPS, as illustrated in Fig. 5(e). The CPF-TCB formed a type II

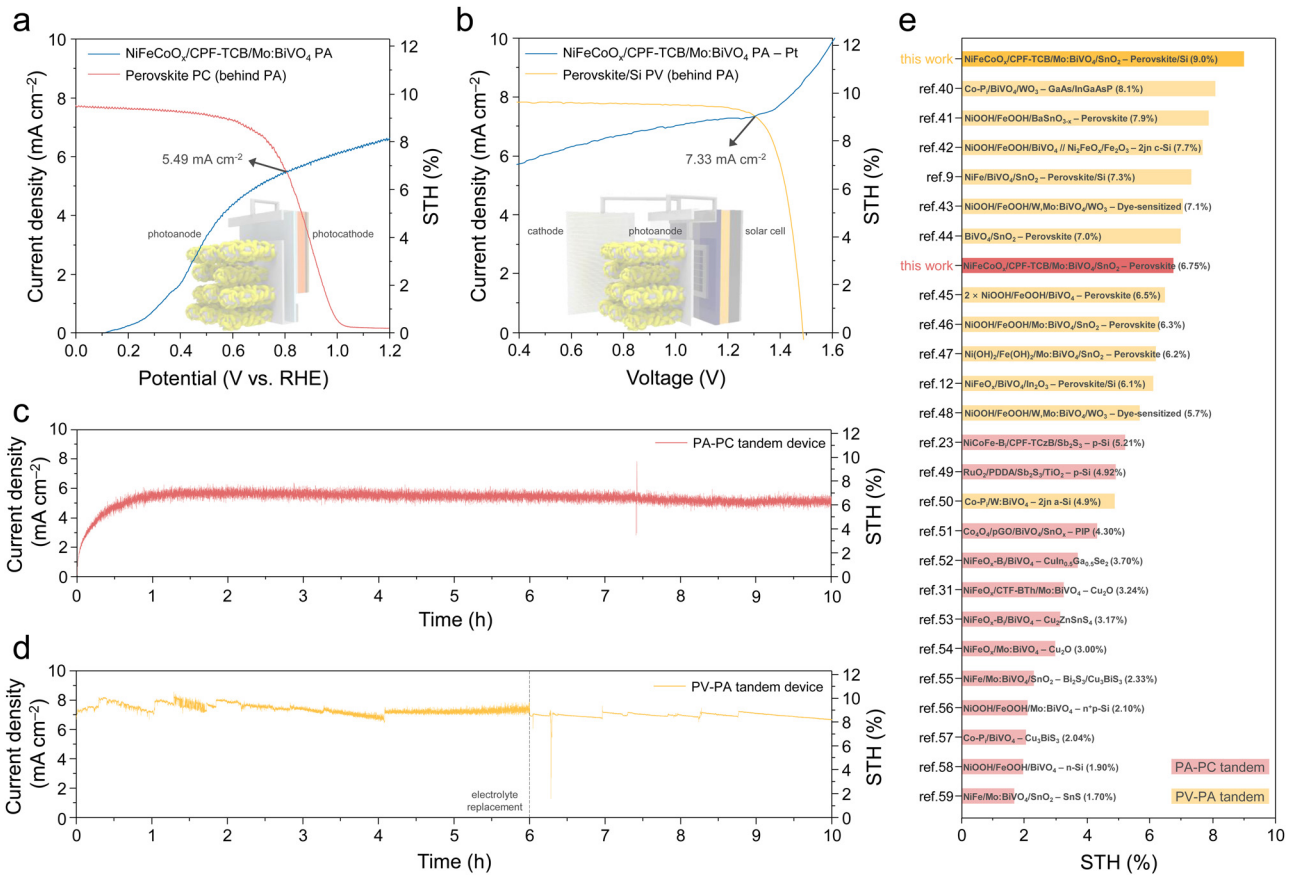

Fig. 6 Unbiased solar hydrogen production. (a) Three-electrode J–V curves of the NiFeCoO$_x$/CPF-TCB/Mo:$BiVO_4$ photoanode and perovskite-based photocathode (behind the photoanode). (b) Two-electrode J–V curves of the NiFeCoO$_x$/CPF-TCB/Mo:$BiVO_4$ photoanode–Pt cathode and perovskite/Si solar cell (behind the photoanode). J–t curves of the (c) unbiased PA–PC and (d) PV–PA tandem devices. (e) STH conversion efficiency benchmarks of the PA–PC and PV–PA tandem devices in mode T. All measurements were conducted in K–B_i buffer (pH 9.5) under AM1.5G 1 sun illumination.

heterojunction with Mo:$BiVO_4$. This band alignment is energetically favorable for not only the efficient extraction of photogenerated holes, but also for blocking photogenerated electrons in Mo:$BiVO_4$, reinforcing the charge separation. As a result, the aforementioned characteristics of CPF-TCB/Mo:$BiVO_4$, such as inhibited charge recombination, rapid hole extraction, and resulting increased carrier concentration, all stem from the band structure.

To implement unbiased solar hydrogen production, the ultimate goal of PEC water splitting, we fabricated two types of tandem devices using the final $NiFeCoO_x$/CPF-TCB/Mo:$BiVO_4$ photoanode. The key requirement for the bottom cell is to avoid overlapping absorption of the photoanode to generate high photocurrent through light harvesting, while being able to generate sufficient photovoltage.[38] Thus, for optimal band gap matching with 2.44 eV of Mo:$BiVO_4$, halide perovskite-based bottom cells were prepared. Firstly, a photoanode–photocathode (PA–PC) tandem device was fabricated by combining the $NiFeCoO_x$/CPF-TCB/Mo:$BiVO_4$ PA and the perovskite PC. The photocathode illustrated in Fig. S16 (ESI†) exhibited prominent PEC performances (photocurrent density of 19.0 mA cm^{-2} at 0 V_{RHE} and onset potential of 1.03 V_{RHE} in potassium phosphate ($K–P_i$) buffer). As shown in Fig. 6(a), the PA–PC tandem device was measured in the $K–B_i$ buffer under tandem illumination mode. The operating current density (J_{OP}) determined by the intersection of 3 electrode *J–V* curves of the PA and PC behind it was 5.49 mA cm^{-2} at 0.81 V_{RHE}., which corresponded to a STH conversion efficiency of 6.75%. Secondly, a photovoltaic–photoanode (PV–PA) tandem device was fabricated by combining the PA and the perovskite/Si solar cell. As displayed in Fig. S17 (ESI†), the PV cell made a similar current density (short-circuit current density of 19.2 mA cm^{-2}) but higher voltages (open-circuit voltage of 1.81 V) compared to photocathodes, since Si generated additional photovoltage by absorbing light transmitted from perovskite.[39] The higher photovoltage allowed the operating point of the PV–PA tandem device to be formed at a higher voltage, delivering a higher J_{OP}. Fig. 6(b) shows the 2-electrode *J–V* curves of the PEC cell comprising a Pt cathode and the $NiFeCoO_x$/CPF-TCB/Mo:$BiVO_4$ PA, and the PV cell behind it under mode T. The J_{OP} of the PV–PA tandem device was 7.33 mA cm^{-2} at 1.30 V, which corresponded to a STH conversion efficiency of 9.02%.

Finally, two fabricated tandem devices were measured by chronoamperometry without an external bias under mode T (Fig. S18, ESI†). As shown in the *J–t* curve (Fig. 6(c)), the PA–PC tandem device recorded a current density that was consistent with the J_{OP} and the corresponding STH conversion efficiency, durably operating for 10 h. Also, the PV–PA tandem device was stably operated for 10 h, generating a current density in accordance with J_{OP} and STH conversion efficiency of 9% (Fig. 6(d)). The PA–PC and PV–PA tandem device we implemented shows the best STH conversion efficiency among each type of tandem device with $BiVO_4$-based photoanodes, as shown in Fig. 6(e). Moreover, it is noteworthy that both types recorded the highest STH conversion efficiency among the mode T tandem devices, which require systematic engineering for the separation of the absorption wavelength (Tables S4 and S5 (ESI†)).[40–59] These results emerge from the high-efficiency tandem device-tailored photoanode, in which a remarkable HTL, CPF-TCB, simultaneously increases the photocurrent and photovoltage of Mo:$BiVO_4$.

Conclusion

We have successfully expedited the hole transport of the nanoporous Mo:$BiVO_4$ photoanode by harnessing a CPF-TCB layer *via* electropolymerization, where the sophisticated control enabled the direct and uniform growth of CPF-TCB without plugging nanopores. Effective charge transport in the CPF-TCB/Mo:$BiVO_4$ heterojunction was disclosed by XANES and XPS analyses, and depth profiling reaffirmed the heterostructure. The planar-averaged charge density difference by the DFT calculations substantiated strong charge separation in CPF-TCB/Mo:$BiVO_4$. Based on the investigation of the charge carrier dynamics, we proved that enhanced hole transport through the CPF-TCB layer suppressed charge recombination and elevated the charge density of the photoanode. Consequently, the $NiFeCoO_x$/CPF-TCB/Mo:$BiVO_4$ photoanode generated an outstanding water oxidation photocurrent density of 6.66 mA cm^{-2} at 1.23 V_{RHE}. Also, its high fill factor played a key role in both types of tandem devices for unassisted solar hydrogen production. The PA–PC tandem device combined with the perovskite photocathode and PV–PA tandem device assembled with perovskite/Si solar cell recorded STH conversion efficiencies of 6.75% and 9.02%, respectively, which are the topmost records among not only $BiVO_4$-based, but also mode T tandem devices. This work broadens the material pool and provides novel strategies for designing high-performance organic–inorganic hybrid photoelectrodes for solar hydrogen production.

Experimental section

Synthesis of nanoporous Mo:$BiVO_4$ photoanodes

SnO_2 NRs as an electron transport layer were fabricated by e-beam evaporation on the FTO glasses with a size of 1 × 1.5 cm^2. After depositing a 50 nm-thick SnO_2 film as an adhesive layer, 2.5 μm-thick SnO_2 NRs were formed with a glancing angle of 85° and a rotation of 80 rpm. Nanoporous Mo:$BiVO_4$ was prepared by the modified two-step electrodeposition on the SnO_2 NRs annealed at 550 °C for 2 h in the air.[9,15] The 50-mL aqueous solution with pH 1.8 contained 0.4 M KI (Daejung, 99.5%), 15 mM $Bi(NO_3)_3{\cdot}5H_2O$ (Junsei, 98%), and 30 mM lactic acid (Sigma-Aldrich, 85%). The 20 mL of ethanol (Daejung, 99.9%)-dissolved 46 mM *p*-benzoquinone (Junsei, 98%) was slowly mixed with the as-prepared solution. After cooling the solution temperature to 22 °C, BiOI was electrodeposited in the three-electrode cell with a Ag/AgCl electrode and Pt mesh. Nucleation of BiOI with a potential of −0.35 $V_{Ag/AgCl}$ for 20 s was followed by its growth with a potential of −0.1 $V_{Ag/AgCl}$ for 4 min. The 10 μL aqueous solution with 0.1 M Na_2MoO_4 (Sigma-Aldrich, 98%) was added into a 5-mL dimethyl sulfoxide

(DMSO) (Kanto, 98%)-dissolved 0.2 M $VO(acac)_2$ (Sigma-Aldrich, 98%) solution. The as-deposited BiOI was converted to Mo:$BiVO_4$ by annealing at 450 °C for 2 h in the air after impregnating the solution. The excess V_2O_5 was removed from the Mo:$BiVO_4$ photoanode by immersing it in 1 M NaOH solution (Daejung) for 10 min.

Surface modification with CPF-TCB hole transport layers and $NiFeCoO_x$ cocatalysts

The CPF-TCB films were fabricated by electropolymerization on Mo:$BiVO_4$ photoanodes. The mixed solvent with 28 mL acetonitrile (Daejung, 99.7%) and 42 mL dichloromethane (Daejung, 99.5%) attained conductivity by dissolving 0.1 M tetrabutylammonium perchlorate (Sigma-Aldrich, 95%). 1,3,5-Tris(*N*-carbazolyl)benzene (4 mM, Sigma-Aldrich, 97%) was dissolved in the solution for 10 min. The potential of the Mo:$BiVO_4$ photoanode in the three-electrode cell with Ag/AgCl and Pt plate was linearly swept in the range of −0.8 to 1.4 $V_{Ag/AgCl}$ with a scan rate of 20 mV s^{-1}. After electropolymerization, the photoanode was rinsed with acetonitrile and ethanol, followed by drying with N_2 flow. The $NiFeCoO_x$ cocatalysts were introduced by dip coating, as modified from previous methods.[12] In a vessel, 2 mL of 10 mM $FeCl_3{\cdot}6H_2O$ (Daejung, 98%), 7 mL of 10 mM $NiCl_2{\cdot}6H_2O$ (Daejung, 96%), and 1 mL of 10 mM $CoCl_2{\cdot}6H_2O$ (Daejung, 97%) solutions were combined and mixed. After immersing the CPF-TCB/Mo:$BiVO_4$ photoanode in the vessel for 15 min, 10 mL of 9 mg L^{-1} tannic acid (Sigma-Aldrich) solution and 75 μL of 2 M NaOH (Daejung, 97%) solution were sequentially added. After 1 h, the photoanode was rinsed with deionized water and dried with N_2 gas flow.

Fabrication of the perovskite photocathodes

The FTO glass was patterned by a laser-etching instrument (Korthem Science), followed by UV treatment for 15 min. As an ETL, the SnO_2 colloidal dispersion (Alfa Aesar) with deionized water (1 : 4; volume ratio) was spin-coated at 3000 rpm for 60 s and heated at 170 °C for 1 h. The perovskite solution was prepared by dissolving 240.8 mg of FAI (Greatcell Solar, 99.99%), 8.25 mg of MABr (Greatcell Solar, 99.99%), 33.76 mg of MACl (Greatcell Solar, 99.99%), 18.19 mg of CsI (Sigma-Aldrich, 99.999%), 705.3 mg of PbI_2 (Sigma-Aldrich, 99.999%), and 27.04 mg of $PbBr_2$ (Sigma-Aldrich, 99.999%) in 0.96 mL of DMF (Sigma-Aldrich, 99.8%) and 0.24 mL DMSO (Sigma-Aldrich, 99.9%) mixed solvent. Subsequently, the solution was stirred for 1 h in an ambient air atmosphere. The perovskite solution was spin-coated at 1200 rpm for 12 s and 5800 rpm for 20 s, followed by annealing at 100 °C for 1 h. An anti-solvent, ethyl acetate (0.8 mL), was dripped onto the substrate for 10 s before the end of the spin-coating process. As an HTL, the spiro-OMeTAD solution comprising 72 mg of spiro-OMeTAD (Sigma-Aldrich, 99%), 8.8 μL of Li-TFSI (Sigma-Aldrich, 99.99%) solution (520 mg of Li-TFSI in 1 mL of acetonitrile), and 4.4 μL of 4-*tert*-butylpyridin (Sigma-Aldrich, 98%) was dissolved in 1 mL of chlorobenzene and spin-coated on the perovskite at 3000 rpm for 60 s. An 80 nm-thick Au top electrode was deposited on the HTL by thermal evaporation. Cu tape and wire were attached to the Au electrode, followed by sealing with an epoxy. Finally, the Pt cocatalyst was deposited on the active area by using a sputter coater (Cressington 108 Auto, Ted Pella).

Fabrication of the perovskite/Si solar cells

The perovskite/Si tandem solar cells were fabricated by the previously reported method.[39] Briefly, on the top of the Si bottom cell with 20 nm-thick of indium tin oxide (ITO) recombination layer, 7 mg mL^{-1} poly(triarylamine) (PTAA, Sigma-Aldrich) solution in toluene was spin-coated at 6000 rpm for 30 s and annealed at 100 °C for 10 min. The 1.3 M perovskite ($Cs_{0.3}DMA_{0.2}MA_{0.5}PbI_3$) solution with 10 mol% of MACl (Lumtec, 99.5%), 1.5 mol% of PEASCN (Greatcell Solar), and 2 mol% of $Pb(SCN)_2$ additives in dimethylformamide (DMF, Sigma-Aldrich, 99.8%) and *N*-methyl-2-pyrroldone (Sigma-Aldrich, 99%) mixed solvent (4 : 1; volume ratio) was spin-coated on PTAA at 3000 rpm for 24 s, and 50 μL of methyl acetate (Sigma-Aldrich, 99%) was dripped at 20 s after the start of spinning, followed by annealing at 100 °C for 10 min. On the perovskite layer, a 15 nm-thick C_{60} (Nano-C) layer was deposited by thermal evaporation, and 0.2 wt% polyethyleneimine (Sigma-Aldrich, 80% ethoxylated) solution in methanol was dynamically spin-coated at 6000 rpm for 30 s. A 40 nm-thick ITO layer was deposited by radio frequency sputtering at room temperature (base pressure: 2×10^{-6} Torr, working pressure: 2×10^{-3} Torr, power: 50 W), and a 500 nm-thick, 50 μm-width Ag grid was deposited by thermal evaporation. Finally, a 105 nm-thick MgF_2 (Sigma-Aldrich, 99.99%) layer was deposited as an anti-reflection layer.

Characterizations

The crystal structures of the samples were identified using XRD (D8 Advance, Bruker) with Cu Kα (1.5406 Å) radiation. The surface morphology and EDX of the samples were investigated by FESEM (MERLIN Compact, ZEISS) with acceleration voltages of 5 and 15 kV, respectively. The HRTEM images and FFT patterns of CPF-TCB/Mo:$BiVO_4$ were analyzed by TEM (JEM-2100F, JEOL) with an acceleration voltage of 200 kV. FT-IR spectra were recorded by FT-IR spectrometer (Nicolet iS50, Thermo Fisher Scientific). The XAS data at V K-edge was obtained on the 7D beamline at the Pohang Light Source (PLS) in the Pohang Accelerator Laboratory (PAL), Republic of Korea. The data were acquired in the fluorescence mode by a solid-state detector and fitted using Athena software (Demeter). The electronic states and chemical compositions were analyzed by XPS (AXIS HSi, KRATOS) with monochromatic Al Kα (1486.6 eV) radiation. Depth profiling was conducted with time variation of Ar ion etching, and the data were fitted using CasaXPS software (CasaXPS). PL spectra were measured at room temperature on the fluorescence spectrometer (FlouTime 300, PicoQuant) with an excitation laser (405 nm). The TRPL data were obtained at the wavelength of 550 nm and fitted with FlouFit software (PicoQuant). Tauc plots were acquired from the absorption spectra calculated by the transmittance and reflectance spectra from the UV-vis spectrometer (V-770,

JASCO). The UPS spectra were measured using XPS (AXIS Nova, KRATOS) with He I (21.22 eV) source.

Photoelectrochemical measurements

A Xe arc lamp (LS 150, Abet Technologies) was used as a light source. Its illumination and intensity were calibrated with AM1.5G filter and Si photodiode (S300, McScience), respectively. The PEC measurements were carried out using a potentiostat (Ivium-n-Stat, Ivium Technologies) in the three-electrode cell with the Ag/AgCl electrode and Pt mesh. Water oxidation of the photoanodes was measured in 1 M K–B_i buffer (pH 9.5), and proton reduction of the perovskite photocathodes was measured in 0.5 M K–P_i buffer (pH 7.0). All of the measured potentials were converted into RHE by the Nernst equation:

$$E_{RHE} = E_{Ag/AgCl} + E^0_{Ag/AgCl} + 0.059 \times pH$$

where $E_{Ag/AgCl}$ is the measured potential (V) *versus* the Ag/AgCl electrode, and $E^0_{Ag/AgCl}$ is 0.198 V at 25 °C. For the *J–V* curves, the potential was swept toward the anodic direction with a scan rate of 20 mV s^{-1} under chopped illumination. The IPCE was measured with separated light by a monochromator (Mono-Ra150i, Dongwoo Optron) at 1.23 V_{RHE}. The current density was calculated by integrating the spectral current density, obtained by multiplying the spectral photon flux by IPCE, over the wavelength. The EIS was recorded from 100 kHz to 1 Hz with an amplitude of 10 mV at 0.5 V_{RHE}. The EIS Nyquist plots were fitted with ZView software (Scribner Associates). The *J–t* curves were recorded at 1.23 V_{RHE}. The gas chromatography system (7890B, Agilent Technologies) was connected to an air-tight H-cell with the photoanode and Pt mesh to calculate the faradaic efficiencies and gas evolution rates at 1.23 V_{RHE}. The M–S plots were recorded at a frequency of 1 kHz with the cathodic potential scan in a dark box. The donor densities were calculated by the slope of the plot. On the open circuit condition, the OCP of the photoanodes was stabilized for 10 min under illumination, and the OCP decay was recorded for the next 10 min after light-off. The OCP-derived carrier lifetimes were calculated by differentiating the OCP with respect to time. The *J–V* curves of the perovskite photocathode were recorded behind the photoanode in the 3-electrode cell with the Ag/AgCl electrode, Pt mesh, and 1 M K–B_i buffer (pH 9.5). After combining the photoanode and photocathode, the *J–t* curve of the PA–PC tandem device was measured under the bias of 0 V. The *J–V* curves of the perovskite/Si solar cells were measured using the potentiostat (CHI 608C, CH Instruments) and the AAA-graded AM1.5G solar simulator (PEC-L11, Peccell Technologies) calibrated by standard Si cell with quartz filter (91150 V, Newport). The *J–V* curves of the 2-electrode cell with the $NiFeCoO_x$/CPF-TCB/Mo:$BiVO_4$ photoanode and Pt cathode were recorded in 1 M K–B_i buffer (pH 9.5), and those of the solar cell were measured behind the photoanode. After connecting the bottom electrode of the solar cell to the photoanode and the top electrode to the cathode, the *J–t* curve of the PV–PA tandem device was measured under the bias of 0 V. The STH conversion efficiencies of the tandem devices were calculated using the following equation:

$$STH\ (\%) = J_{OP} \times 1.23 \times \eta_F / P_{in}$$

where J_{OP} is the operating photocurrent density (mA cm^{-2}), η_F is the faradaic efficiency, and P_{in} is an incident solar power (100 mW cm^{-2}).

Computational details

The spin-polarized DFT calculations were performed using the Vienna Ab initio Simulation Package (VASP) with the projector-augmented wave method for the core region and a plane-wave kinetic energy cutoff of 400 eV. The generalized gradient approximation (GGA) in the form of Perdew–Burke–Ernzerhof (PBE) for the exchange–correlation potentials was used. The DFT+*U* calculations were performed with Hubbard–*U* correction of $U = 3.25$ eV to the d-electrons of Bi to account for the on-site correlation effects. A 7 × 5 × 7 gamma-centered Monkhorst–pack sampled *k*-point grid was employed to sample the reciprocal space for the bulk $BiVO_4$. Monkhorst–pack *k*-point meshes of 2 × 2 × 1 were used for structure optimization and property calculation of the $BiVO_4$ (010) slab, CPF-TCB, and the heterojunction CPF-TCB/$BiVO_4$ (010) heterostructure. The large vacuum layers of these slab models were set at least 15 Å in the *z*-direction for the isolation of the surface to prevent the interaction between two periodic units. The optimized lattice constants of $BiVO_4$ were $a = 7.338$ Å, $b = 11.727$ Å, $c = 5.188$ Å, $\alpha = \gamma = 90.00°$, and $\beta = 135.01°$, respectively. The surface of $BiVO_4$ (010) was carried out using the slab model composed of $p(4 \times 3)$ supercells with four metal atomic monolayers. The bottom two atomic monolayers of $BiVO_4$ (010) were fixed at their bulk positions, while the remaining atomic layers and 2-dimensional CPF-TCB layer were free to move in all directions until the convergence of energy and residual force on each atom were less than 1×10^{-4} eV and 0.05 eV $Å^{-1}$, respectively. To describe the charge transfer process in the CPF-TCB/$BiVO_4$ heterostructure, the dipole moment on the *z*-direction was calculated, and the planar-averaged charge density was acquired by averaging the charge density on the *xy* plane toward the *z*-direction.

Data availability

All data supporting the findings of this study are available within the main text and the ESI.† All relevant data are available from the corresponding authors upon reasonable request.

Author contributions

H. W. J., J. Y. K., J. M., and M. S. K. supervised the project. H. W. J. and J. W. Y. conceived the project and designed the experiments. J. W. Y. fabricated and measured the devices, and analyzed the experimental results. S. G. J. fabricated the perovskite/Si solar cells. C. S. J. fabricated the perovskite photocathodes. J. K. performed the density functional theory calculations and helped to analyze the X-ray absorption spectra. H. R. K. helped to analyze the carrier dynamics. T. H. L. carried out the transmission electron microscopic characterizations.

S. A. L. helped to analyze the experimental results. W. S. C. conducted gas chromatography measurements. S. L. helped to synthesize conjugated polymers. H. L. helped to measure the photocathode. J. W. Y. and H. W. J. mainly wrote the manuscript. All authors discussed the results and commented on the manuscript at all stages.

Conflicts of interest

The authors declare no competing interests.

Acknowledgements

This research was supported by the National Research Foundation of Korea (NRF) grant funded by the Korea government Ministry of Science and ICT (MSIT) (2021R1A2B5B03001851, 2021M3H4A1A03057403). This work was also supported by the KRISS (Korea Research Institute of Standards and Science) MPI Lab. program. H. W. J. gratefully acknowledges the KRISS MPI Lab. program. J. W. Y. acknowledges the NRF grant funded by the Korea government MSIT (RS-2023-00213786). The Inter-University Semiconductor Research Center and Institute of Engineering Research at Seoul National University provided research facilities for this work. We thank the Pohang Accelerator Laboratory for providing the synchrotron radiation source at the 7D beamline.

References

1 M. Grätzel, *Nature*, 2001, **414**, 338–344.
2 V. Andrei, G. M. Ucoski, C. Pornrungroj, C. Uswachoke, Q. Wang, D. S. Achilleos, H. Kasap, K. P. Sokol, R. A. Jagt, H. Lu, T. Lawson, A. Wagner, S. D. Pike, D. S. Wright, R. L. Z. Hoye, J. L. MacManus-Driscoll, H. J. Joyce, R. H. Friend and E. Reisner, *Nature*, 2022, **608**, 518–522.
3 I. Roger, M. A. Shipman and M. D. Symes, *Nat. Rev. Chem.*, 2017, **1**, 0003.
4 K. Sivula and R. Van De Krol, *Nat. Rev. Mater.*, 2016, **1**, 15010.
5 W. Yang, R. R. Prabhakar, J. Tan, S. D. Tilley and J. Moon, *Chem. Soc. Rev.*, 2019, **48**, 4979–5015.
6 T. W. Kim and K. S. Choi, *Science*, 2014, **343**, 990–994.
7 D. K. Lee and K. S. Choi, *Nat. Energy*, 2018, **3**, 53–60.
8 S. Corby, R. R. Rao, L. Steier and J. R. Durrant, *Nat. Rev. Mater.*, 2021, **6**, 1136–1155.
9 J. W. Yang, I. J. Park, S. A. Lee, M. G. Lee, T. H. Lee, H. Park, C. Kim, J. Park, J. Moon, J. Y. Kim and H. W. Jang, *Appl. Catal., B*, 2021, **293**, 120217.
10 M. J. Choi, T. L. Kim, K. S. Choi, W. Sohn, T. H. Lee, S. A. Lee, H. Park, S. Y. Jeong, J. W. Yang, S. Lee and H. W. Jang, *ACS Appl. Mater. Interfaces*, 2022, **14**, 7788–7795.
11 M. G. Lee, J. W. Yang, H. Park, C. W. Moon, D. M. Andoshe, J. Park, C. K. Moon, T. H. Lee, K. S. Choi, W. S. Cheon, J. J. Kim and H. W. Jang, *Nano-Micro Lett.*, 2022, **14**, 48.
12 M. G. Lee, J. W. Yang, I. J. Park, T. H. Lee, H. Park, W. S. Cheon, S. A. Lee, H. Lee, S. G. Ji, J. M. Suh, J. Moon, J. Y. Kim and H. W. Jang, *Carbon Energy*, 2023, **5**, e321.
13 K. H. Ye, Z. Wang, J. Gu, S. Xiao, Y. Yuan, Y. Zhu, Y. Zhang, W. Mai and S. Yang, *Energy Environ. Sci.*, 2017, **10**, 772–779.
14 B. Jin, Y. Cho, C. Park, J. Jeong, S. Kim, J. Jin, W. Kim, L. Wang, S. Lu, S. Zhang, S. H. Oh, K. Zhang and J. H. Park, *Energy Environ. Sci.*, 2022, **15**, 672–679.
15 K. H. Ye, H. Li, D. Huang, S. Xiao, W. Qiu, M. Li, Y. Hu, W. Mai, H. Ji and S. Yang, *Nat. Commun.*, 2019, **10**, 3687.
16 S. Gu, H. Neugebauer and N. S. Sariciftci, *Chem. Rev.*, 2007, **107**, 1324–1338.
17 D. Xu, Z. Gong, Y. Jiang, Y. Feng, Z. Wang, X. Gao, X. Lu, G. Zhou, J. M. Liu and J. Gao, *Nat. Commun.*, 2022, **13**, 7020.
18 K. Jinnai, R. Kabe, Z. Lin and C. Adachi, *Nat. Mater.*, 2022, **21**, 338–344.
19 L. R. MacFarlane, H. Shaikh, J. D. Garcia-Hernandez, M. Vespa, T. Fukui and I. Manners, *Nat. Rev. Mater.*, 2021, **6**, 7–26.
20 Q. Chen, M. Luo, P. Hammershøj, D. Zhou, Y. Han, B. W. Laursen, C. G. Yan and B. H. Han, *J. Am. Chem. Soc.*, 2012, **134**, 6084–6087.
21 K. Takagi, H. Takao and T. Nakagawa, *Polym. J.*, 2013, **45**, 396–400.
22 Z. Zhou, X. Li, D. Guo, D. B. Shinde, D. Lu, L. Chen, X. Liu, L. Cao, A. M. Aboalsaud, Y. Hu and Z. Lai, *Nat. Commun.*, 2020, **11**, 5323.
23 L. Wang, W. Lian, B. Liu, H. Lv, Y. Zhang, X. Wu, T. Wang, J. Gong, T. Chen and H. Xu, *Adv. Mater.*, 2022, **34**, 2200723.
24 M. G. Lee, J. W. Yang, H. R. Kwon and H. W. Jang, *CrystEngComm*, 2022, **24**, 5838–5864.
25 B. Liu, S. Wang, G. Zhang, Z. Gong, B. Wu, T. Wang and J. Gong, *Chem. Soc. Rev.*, 2023, **52**, 4644–4671.
26 J. Chen, C. L. Dong, D. Zhao, Y. C. Huang, X. Wang, L. Samad, L. Dang, M. Shearer, S. Shen and L. Guo, *Adv. Mater.*, 2017, **29**, 1606198.
27 K. Zhang, B. Jin, C. Park, Y. Cho, X. Song, X. Shi, S. Zhang, W. Kim, H. Zeng and J. H. Park, *Nat. Commun.*, 2019, **10**, 2001.
28 M. Zhu, Z. Sun, M. Fujitsuka and T. Majima, *Angew. Chem., Int. Ed.*, 2018, **130**, 2182–2186.
29 M. Huang, Z. Huang and H. Zhu, *Nano Energy*, 2020, **70**, 104487.
30 Y. Shi, Y. Yu, Y. Liang, Y. Du and B. Zhang, *Angew. Chem., Int. Ed.*, 2019, **131**, 3809–3813.
31 Y. Zhang, H. Lv, Z. Zhang, L. Wang, X. Wu and H. Xu, *Adv. Mater.*, 2021, **33**, 2008264.
32 J. Li, L. Cai, J. Shang, Y. Yu and L. Zhang, *Adv. Mater.*, 2016, **28**, 4059–4064.
33 H. Zhang, D. Li, W. J. Byun, X. Wang, T. J. Shin, H. Y. Jeong, H. Han, C. Li and J. S. Lee, *Nat. Commun.*, 2020, **11**, 4622.
34 M. Zhong, T. Hisatomi, Y. Kuang, J. Zhao, M. Liu, A. Iwase, Q. Jia, H. Nishiyama, T. Minegishi, M. Nakabayashi, N. Shibata, R. Niishiro, C. Katayama, H. Shibano, M. Katayama, A. Kudo, T. Yamada and K. Domen, *J. Am. Chem. Soc.*, 2015, **137**, 5053–5060.

35 Y. Lin, Y. Xu, M. T. Mayer, Z. I. Simpson, G. McMahon, S. Zhou and D. Wang, *J. Am. Chem. Soc.*, 2012, **134**, 5508–5511.
36 B. Liu, X. Wang, Y. Zhang, L. Xu, T. Wang, X. Xiao, S. Wang, L. Wang and W. Huang, *Angew. Chem., Int. Ed.*, 2023, **135**, e202217346.
37 S. Wang, T. He, P. Chen, A. Du, K. Ostrikov, W. Huang and L. Wang, *Adv. Mater.*, 2020, **32**, 2001385.
38 J. H. Kim, D. Hansora, P. Sharma, J. W. Jang and J. S. Lee, *Chem. Soc. Rev.*, 2019, **48**, 1908–1971.
39 S. G. Ji, I. J. Park, H. Chang, J. H. Park, G. P. Hong, B. K. Choi, J. H. Jang, Y. J. Choi, H. W. Lim, Y. J. Ahn, S. J. Park, K. T. Nam, T. Hyeon, J. Park, D. H. Kim and J. Y. Kim, *Joule*, 2022, **6**, 2390–2405.
40 Y. Pihosh, I. Turkevych, K. Mawatari, J. Uemura, Y. Kazoe, S. Kosar, K. Makita, T. Sugaya, T. Matsui, D. Fujita, M. Tosa, M. Kondo and T. Kitamori, *Sci. Rep.*, 2015, **5**, 11141.
41 M. Kim, B. Lee, H. Ju, J. Y. Kim, J. Kim and S. W. Lee, *Adv. Mater.*, 2019, **31**, 1903316.
42 J. H. Kim, J. W. Jang, Y. H. Jo, F. F. Abdi, Y. H. Lee, R. Van De Krol and J. S. Lee, *Nat. Commun.*, 2016, **7**, 13380.
43 X. Shi, H. Jeong, S. J. Oh, M. Ma, K. Zhang, J. Kwon, I. T. Choi, I. Y. Choi, H. K. Kim, J. K. Kim and J. H. Park, *Nat. Commun.*, 2016, **7**, 11943.
44 Z. Xu, L. Chen, C. J. Brabec and F. Guo, *Small Methods*, 2023, **7**, 2300619.
45 S. Wang, P. Chen, Y. Bai, J. H. Yun, G. Liu and L. Wang, *Adv. Mater.*, 2018, **30**, 1800486.
46 S. Xiao, C. Hu, H. Lin, X. Meng, Y. Bai, T. Zhang, Y. Yang, Y. Qu, K. Yan, J. Xu, Y. Qiu and S. Yang, *J. Mater. Chem. A*, 2017, **5**, 19091–19097.
47 Y. Qiu, W. Liu, W. Chen, G. Zhou, P. C. Hsu, R. Zhang, Z. Liang, S. Fan, Y. Zhang and Y. Cui, *Sci. Adv.*, 2016, **2**, 1501764.
48 X. Shi, K. Zhang, K. Shin, M. Ma, J. Kwon, I. T. Choi, J. K. Kim, H. K. Kim, D. H. Wang and J. H. Park, *Nano Energy*, 2015, **13**, 182–191.
49 Y. S. Park, X. Jin, J. Tan, H. Lee, J. Yun, S. Ma, G. Jang, T. Kim, S. G. Shim, K. Kim, J. Lee, C. U. Lee, S. J. Hwang and J. Moon, *Energy Environ. Sci.*, 2022, **15**, 4725–4737.
50 F. F. Abdi, L. Han, A. H. M. Smets, M. Zeman, B. Dam and R. Van De Krol, *Nat. Commun.*, 2013, **4**, 2195.
51 S. Ye, W. Shi, Y. Liu, D. Li, H. Yin, H. Chi, Y. Luo, N. Ta, F. Fan, X. Wang and C. Li, *J. Am. Chem. Soc.*, 2021, **143**, 12499–12508.
52 H. Kobayashi, N. Sato, M. Orita, Y. Kuang, H. Kaneko, T. Minegishi, T. Yamada and K. Domen, *Energy Environ. Sci.*, 2018, **11**, 3003–3009.
53 D. Huang, K. Wang, L. Li, K. Feng, N. An, S. Ikeda, Y. Kuang, Y. Ng and F. Jiang, *Energy Environ. Sci.*, 2021, **14**, 1480–1489.
54 L. Pan, J. H. Kim, M. T. Mayer, M. K. Son, A. Ummadisingu, J. S. Lee, A. Hagfeldt, J. Luo and M. Grätzel, *Nat. Catal.*, 2018, **1**, 412–420.
55 S. Moon, J. Park, H. Lee, J. W. Yang, J. Yun, Y. S. Park, J. Lee, H. Im, H. W. Jang, W. Yang and J. Moon, *Adv. Sci.*, 2023, **10**, 2206286.
56 W. Vijselaar, P. Westerik, J. Veerbeek, R. M. Tiggelaar, E. Berenschot, N. R. Tas, H. Gardeniers and J. Huskens, *Nat. Energy*, 2018, **3**, 185–192.
57 D. Huang, L. Li, K. Wang, Y. Li, K. Feng and F. Jiang, *Nat. Commun.*, 2021, **12**, 3795.
58 B. Liu, S. Feng, L. Yang, C. Li, Z. Luo, T. Wang and J. Gong, *Energy Environ. Sci.*, 2020, **13**, 221–228.
59 H. Lee, J. W. Yang, J. Tan, J. Park, S. G. Shim, Y. S. Park, J. Yun, K. Kim, H. W. Jang and J. Moon, *Adv. Sci.*, 2021, **8**, 2102458.